Space Target 3-D Reconstruction Using Votes Accumulation Method of ISAR Image Sequence

Dan Xu, Xuan Wang, Zhixin Wu, *Graduate Student Member, IEEE*, Jixiang Fu, *Member, IEEE*, Yuhong Zhang, Jianlai Chen, *Senior Member, IEEE*, and Mengdao Xing, *Fellow, IEEE*

***Abstract*—Combining inverse projection and vote accumulation methods, we propose a novel 3-D geometric reconstruction method based on inverse synthetic aperture radar image sequence for triaxially stabilized space targets. Considering that the translation of a triaxially stabilized space target results in a large angular rotation of the radar line-of-sight and an attitude adjustment rotation of the target itself, the projection relationship between the radar imaging plane and a triaxially stabilized space target is constructed first. Subsequently, we perform an inverse projection on the dominant points extracted from each imaging plane to determine the location of the 3-D candidate scatterers and assign a voting value of 1 to each position. By accumulating these vote values, we can obtain the total number of votes for the candidate scatterer position. We treat candidate 3-D scatterers with a large cumulative number of votes as actual scatterers. Thus, the target 3-D geometry can be obtained. Compared with the traditional matrix factorization-based 3-D reconstruction methods, this method is more accurate and ensures that the target pose is consistent with the actual pose. At the same time, compared with 3-D reconstruction methods based on the energy accumulation ideas, this method produces fewer false scatterers and has higher credibility. The experimental results based on the simulated point target and electromagnetic data are presented to validate the effectiveness and robustness of the proposed method.**

***Index Terms*—3-D geometric reconstruction, image sequence, inverse synthetic aperture radar (ISAR), vote accumulation.**

Manuscript received 6 January 2024; revised 29 March 2024; accepted 7 May 2024. Date of publication 20 May 2024; date of current version 30 May 2024. This work was supported in part by the Fundamental Research Funds for the Central Universities under Grant ZYTS24126, in part by the Open Fund of Laboratory of Pinghu, in part by the National Natural Science Foundation of China under Grant 62371468, in part by the Young Scientist Fund of the National Natural Science Foundation of China under Grant 62301389, and in part by the Natural Science Foundation of Fujian Province under Grant 2023J05300, Grant 2023J01242, and Grant 2023J011801. *(Corresponding authors: Jixiang Fu; Mengdao Xing.)*

Dan Xu and Jixiang Fu are with the Academy of Advanced Interdisciplinary Research, Xidian University, Xi'an 710071, China (e-mail: danxu@xidian.edu.cn; jxfu@xidian.edu.cn).

Xuan Wang is with the School of Optoelectronic Engineering, Xidian University, Xi'an 710071, China (e-mail: wx@stu.xidian.edu.cn).

Zhixin Wu is with the National Key Laboratory of Radar Signal Processing, Xidian University, Xi'an 710071, China (e-mail: zhixin_wu@stu.xidian.edu.cn).

Yuhong Zhang is with the School of Electronic Information, Xi'an Polytechnic University, Xi'an 710048, China (e-mail: xiaoshan198717@163.com).

Jianlai Chen is with the School of Automation, Central South University, Changsha 410083, China (e-mail: jianlaichen@163.com).

Mengdao Xing is with the National Laboratory of Radar Signal Processing, Xidian University, Xi'an 710071, China, and also with the Collaborative Innovation Center of Information Sensing and Understanding, Xidian University, Xi'an 710071, China (e-mail: xmd@xidian.edu.cn).

Digital Object Identifier 10.1109/JSTARS.2024.3401707

I. Introduction

With the development of inverse synthetic aperture radar (ISAR) application in space non-cooperative targets, besides its all-day and all-weather operation capability, ISAR has been widely utilized in military and civil areas [1], [2], [3], [4]. In general, the 2-D ISAR image is the projection of the target 3-D geometry structure onto the radar imaging plane. Because space exploration requires not only the acquisition of satellite sizes but also the acquisition of satellite working status, space satellite pointing, and the recovery of faulty satellites [5], [6], [7], [8], [9]. The 3-D image contains abundant information about the target's structure and size. Moreover, it plays a crucial role in automatic object classification and recognition in radar applications. Therefore, 3-D geometric reconstruction has received significant attention in recent years [10], [11].

According to the existing algorithms, 3-D geometric reconstruction algorithms can be roughly fallen into three categories: interferometric ISAR(InISAR), multiple-input multiple-output ISAR(MIMO-ISAR), and 3-D reconstruction based on monostatic ISAR.

The first category is based on InISAR, which needs multiple sensors in a special coordinate configuration to acquire 3-D image of moving targets [12], [13], [14], [15]. In an InISAR system, interferometry is performed by using the interferometric phase of ISAR images from multiple sensors. In addition, the InISAR system can quickly and easily obtain 3-D images without knowing the prior motion parameters of the target. However, the superior performance of the InISAR system comes with costly equipment and complex configurations.

The second category is based on frequency diversity-distributed MIMO-ISAR [16], [17], [18]. A distributed radar consists of transmit and receive stations according to different distributions, which can be implemented by a MIMO radar system. MIMO-ISAR combines the features of real aperture imaging for MIMO radar and synthetic aperture imaging for ISAR. Therefore, MIMO-ISAR not only reduces the time for ISAR imaging accumulation but also reduces the number of real array elements for MIMO radar imaging. However, the well-performing MIMO-ISAR and InISAR techniques are not suitable for monostatic ISAR.

The third category is 3-D reconstruction based on monostatic ISAR [19], [20], [21], [22], [23], [24]. In [19], a monostatic ISAR approach is employed to obtain the target's 3-D image with sufficient measurements in three dimensions. However, this

method has a significant drawback as it requires the target to be stationary while the radar moves along a predetermined trajectory, rendering it impractical for real-world scenarios where such conditions cannot be met. In [20], the target's 3-D structure and motion are estimated from high-resolution range profiles. Although this approach does not require any prior knowledge of the target geometry, its effectiveness diminishes when multiple scatterers are present and interconnected within a single range cell. However, this issue can be resolved by utilizing ISAR image sequences [21], [22], [23], [24], [25], [26], [27], [28], [29]. By analyzing the projection relationship between the 2-D image sequence and the target 3-D geometry, the target 3-D reconstruction can be obtained via matrix factorization algorithm (MFA) [28], [29]. In these methods, the first step is to extract and associate dominant scatterers from sequential ISAR images to form a trajectory matrix. Then, 3-D reconstruction can be obtained by factorizing the trajectory matrix. However, during the process, the cross-range scaling should be performed accurately to each subimage and associating the scatterers extracted from these images, which is a time-consuming operation. Besides, due to the anisotropy of radar cross sections, the number of scatterers that can be associated decreases sharply with the increase of subapertures. In [30], the target 3-D reconstruction can be obtained based on the ISAR image sequence energy accumulation (ISEA). This method never needs the 2-D scatterer extraction and trajectory association. However, this approach is highly time-consuming and requires a high signal-to-noise ratio (SNR) as the true 3-D scatterers are obtained by searching energy accumulation for 3-D scatterer candidates one by one.

To relax the strict condition of multiview continuous matching of scatterers and the influence of low SNR, this article proposes a novel 3-D reconstruction for triaxially stabilized space targets. Triaxially stabilized space targets with stable orbits generally undergo steady motion. Therefore, ISAR can obtain long-time, wide-angle target echoes. We first generate high-resolution image sequence by dividing echo data into overlapped subapertures and obtain high-resolution 2-D images [30], [31], [32], [33]. Then, driven by the fact that the projected position of a real scatterer will yield higher energy in the 2-D image than a fake scatterer induced by noise or energy leakage. Moreover, it is unlikely that the noise appears continuously at the corresponding positions of the sequence. Occasionally, certain images exhibit exceptionally high noise intensity, surpassing that of weak real scatterers and resulting in a considerable accumulation of energy from this noise. Such noise can create significant clutter in energy-based 3-D reconstructions. Conversely, the voting method has proven effective in reducing noise interference and relaxing the rigorous requirements of sequence alignment.

Based on the above analysis, we detect and extract features from 2-D images. The extracted scatterers are the projected positions of the candidate scatterers, and their corresponding votes are set as one. We can analyze the score distribution of a sequence of ISAR images and accumulate votes along the projected position of a 3-D scatterer candidate. As a result, the vote score of the real 3-D scatterers will be considerably larger than the fake ones. The projection relation is the same for the projected positions from the same imaging plane. The 3-D positions of all target scatterers can be computed at once by backprojection. In the article, the accuracy of the 3-D reconstruction and the validity of the reconstructed structures are evaluated using the methods of minimum mean square error, false possible rate, and false negative rate. These evaluation results fully demonstrate the robustness and effectiveness of the proposed algorithm.

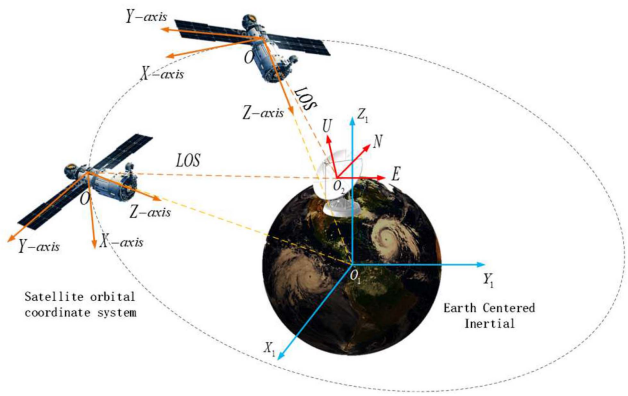

Fig. 1. Radar observation model of the satellite in orbit.

The rest of this article is organized as follows. In Section II, we first give a detailed introduction to the projective theory of space targets. In Section III, the vote accumulation method is introduced to achieve the matching of multiple incomplete point groups. Section IV compares and analyzes the results of the experiments. Three 3-D reconstruction methods are used to validate the effectiveness and superiority of the proposed method. Section V gives a summary and analysis. Finally, Section VI concludes this article.

II. Space Target Observation and ISAR Imaging Model

In ISAR imaging, space targets are non-cooperative targets. Therefore, the motion features are unknown in advance. However, for triaxially stabilized space targets, the attitude remains stationary with respect to the orbital coordinate system. Since the attitude of the triaxially stabilized space target remains fixed with respect to the orbital coordinate system, we assume that the satellite is continuously facing the Earth at some point during the observation. When a satellite appears on the radar line-of-sight (LOS) and is within range of the radar, the radar starts tracking and observing the satellite until the satellite is out of the radar field of view, as shown in Fig. 1. Here, we can see three coordinates' systems, namely, the satellite orbital coordinate system, the geocentric coordinate system, and the radar coordinate system. $O-XYZ$ represents the satellite orbital coordinate system, where O is the target center and the OZ coordinates are oriented from the target center to the Earth center. The target orbital plane is formulated in terms of the OZ coordinates and the direction of the target motion. In the same direction, the OX-axis lies in the orbital plane and is perpendicular to the OZ-axis. The OY-axis is determined by the right-hand rule. $O_1-X_1Y_1Z_1$ denotes the Earth-centered Earth-fixed (ECEF) coordinate system, where O_1 is the Earth center and O_1Z_1

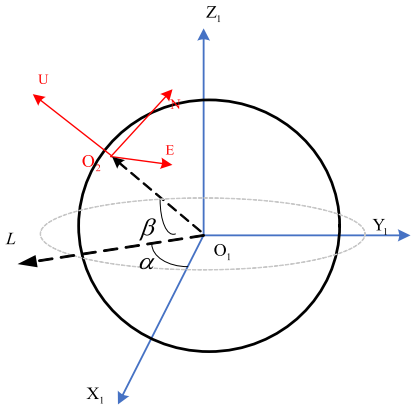

Fig. 2. Relation between the radar coordinate system and the ECEF coordinate system.

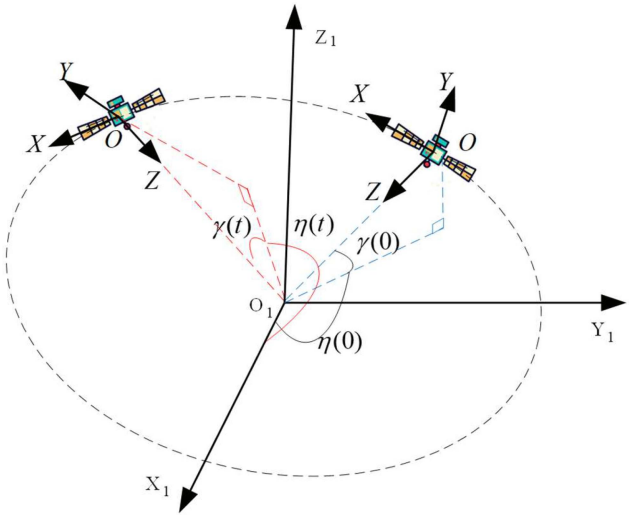

Fig. 3. Attitude of space target in the ECEF coordinate system.

is oriented toward the north pole. The O_1X_1-axis lies in the plane of the equator and points toward the equinox. The O_1Y_1 is determined by the right-hand rule. $O_2 - UNE$ is the radar coordinate system, which is set in conjunction with the location of the radar transceiver antenna. O_2 represents the origin of the radar coordinate system. The plane formed by O_2E and O_2N is tangent to the Earth surface. The O_2E axis is oriented eastward along the latitude. The O_2N axis is oriented north along the longitude. The O_2U is determined by the right-hand rule.

By analyzing the relative relationship among the moving space target, the Earth, and the radar, we conclude that the rotation of the space target with respect to the radar consists of two parts, namely the orbit motion and the attitude adjustment motion. The orbital motion angle of the satellite with respect to the radar varies by more than 90°. At the same time, the Earth's rotation is negligible compared to it, at about 1°. Generally, the orbital motion is reflected in the shift of radar LOS. The instantaneous LOS can be described by observation angles, shown as follows:

$$\mathbf{l}_{\text{ob}}(t) = [\cos\varphi_r(t)\cos\theta_r(t), \sin\varphi_r(t)\cos\theta_r(t), \sin\theta_r(t)]^T \tag{1}$$

where t is the observation time, and $\theta_r(t)$ and $\varphi_r(t)$ denote the instantaneous elevation angle and azimuth angle, respectively. The position of the satellite in the radar coordinate system can be represented as

$$\mathbf{P}_{\text{radar}}(t) = r_0(t)\mathbf{l}_{\text{ob}}(t) \tag{2}$$

where $r_0(t)$ is the distance from the satellite to the radar.

As shown in Fig. 2, assume that the latitude and longitude of the radar position are α and β, respectively, where O_1L is the projection of the longitude of the radar position in the equatorial plane. Then, the location of the radar in the Earth's coordinate system is

$$\mathbf{r} = R_e[\cos\beta\cos\alpha, \cos\beta\sin\alpha, \sin\beta]^T \tag{3}$$

where R_e denotes the radius of the Earth. Then, the instantaneous position of the space target in the Earth-centered inertial coordinate system can be expressed as

$$\mathbf{P}_{\text{earth}}(t) = \mathbf{T_1}\cdot\mathbf{P}_{\text{radar}}(t) + \mathbf{r} = [X_{\text{earth}}(t), Y_{\text{earth}}(t), Z_{\text{earth}}(t)] \tag{4}$$

where $\mathbf{T_1}$ denotes the transformation from the radar coordinate system to the ECEF coordinate system, expressed as

$$\mathbf{T}_1 = \begin{bmatrix} \sin\alpha & -\cos\alpha\sin\beta & \cos\alpha\sin\beta \\ \cos\alpha & \sin\alpha\sin\beta & -\sin\alpha\cos\beta \\ 0 & \cos\beta & \sin\beta \end{bmatrix}. \tag{5}$$

The triaxially stabilized space target is fixed in the orbit coordinate system. Considering that the *OZ*-axis always points to the center of the Earth, the attitude changes of the space target in the ECEF coordinate system are exactly opposite to the position change in the ECEF coordinate system, as shown in Fig. 3. The variation of scattering points on the satellite relative to the ECEF coordinate system can be expressed using azimuth angle $\eta(t)$ and elevation angle $\gamma(t)$, which are described as follows:

$$\eta(t) = \begin{cases} \arccos\left(\dfrac{X_{\text{earth}}(t)}{\sqrt{(X_{\text{earth}}(t)+Y_{\text{earth}}(t))^2}}\right), & Y_{\text{earth}}(t) > 0 \\ 2\pi - \arccos\left(\dfrac{X_{\text{earth}}(t)}{\sqrt{(X_{\text{earth}}(t)+Y_{\text{earth}}(t))^2}}\right), & Y_{\text{earth}}(t) < 0 \end{cases} \tag{6}$$

$$\gamma(t) = \arctan\left(\frac{Z_{\text{earth}}(t)}{\sqrt{(X_{\text{earth}}(t)+Y_{\text{earth}}(t))^2}}\right), \quad \gamma(t) \in (-\pi/2, \pi/2). \tag{7}$$

The rotation matrix due to the space target attitude adjustment in the ECEF coordinate system can be acquired as

$$\mathbf{T}_2(t) = A_t^{-1}\cdot A_0 \tag{8}$$

where A_t^{-1} and A_0 denote the attitude changes of space target in the ECEF coordinate system, denoted as

$$\begin{cases} A_t^{-1} = \begin{bmatrix} 1 & 0 & 0 \\ 0 & \cos(\gamma(t)) & \sin(\gamma(t)) \\ 0 & -\sin(\gamma(t)) & \cos(\gamma(t)) \end{bmatrix} \\ \quad \cdot \begin{bmatrix} \cos(\eta(t)) & \sin(\eta(t)) & 0 \\ -\sin(\eta(t)) & \cos(\eta(t)) & 0 \\ 0 & 0 & 1 \end{bmatrix} \\ A_0 = \begin{bmatrix} \cos(\eta(0)) & -\sin(\eta(0)) & 0 \\ \sin(\eta(0)) & \cos(\eta(0)) & 0 \\ 0 & 0 & 1 \end{bmatrix} \\ \quad \cdot \begin{bmatrix} 1 & 0 & 0 \\ 0 & \cos(\gamma(0)) & -\sin(\gamma(0)) \\ 0 & \sin(\gamma(0)) & \cos(\gamma(0)) \end{bmatrix}. \end{cases} \tag{9}$$

Suppose that a point on the target is denoted by $\mathbf{p}_{0n} = [x_n, y_n, z_n]^T$ at initial time. After compensating for translation, taking into account both orbital motion and attitude adjustment, the displacement of the scatterer with respect to the radar is denoted by

$$\mathbf{p}_n(t) = \mathbf{T}_1^{-1} \cdot \mathbf{T}_2(t) \cdot \mathbf{T}_1 \cdot \mathbf{p}_{0n}. \tag{10}$$

Therefore, the instantaneous absolute LOS can be expressed as

$$\mathbf{l}_e(t) = {\mathbf{T}_1}^T \cdot {\mathbf{T}_2}^T(t) \cdot \left(\mathbf{T}_1^{-1}\right)^T \mathbf{l}_{\text{ob}}(t). \tag{11}$$

Combining (10) and (11), the projected position of $\mathbf{p}_{0n}$ along the instantaneous absolute LOS can be obtained as

$$r_n(t) = \mathbf{p}_{0n} \cdot \mathbf{l}_e(t). \tag{12}$$

The cross-range coordinate of the scatterer can be expressed as

$$f_n(t) = -\frac{2}{\lambda} \cdot \frac{\partial r_n(t)}{\partial t} \tag{13}$$

where λ is the wavelength.

During long-duration, large-angle satellite observations, the radar imaging plane undergoes changes. To simplify the imaging plane, subview division is adopted to split the original large rotation angle into multiple small subviews. Within each small subview, the imaging plane can be approximately considered as constant, as shown in Fig. 4. Supposing long-time ISAR echo is divided into K overlapped subapertures, the image projection plane of the kth subaperture can be defined by the range projection vector r_k and the Doppler projection vector $f_{a,k}$, expressed as

$$\begin{cases} r_k = [\cos\varphi(t_k)\cos\theta(t_k), \sin\varphi(t_k)\cos\theta(t_k), \sin\theta(t_k)]^T \\ f_{a,k} = \frac{2}{\lambda} \cdot \begin{bmatrix} \dot{\theta}(t_k)\cos\varphi(t_k)\sin\theta(t_k) \\ +\dot{\varphi}(t_k)\sin\varphi(t_k)\cos\theta(t_k) \\ \dot{\theta}(t_k)\sin\varphi(t_k)\sin\theta(t_k) \\ -\dot{\varphi}(t_k)\cos\varphi(t_k)\cos\theta(t_k) \\ -\dot{\theta}(t_k)\cos\theta(t_k) \end{bmatrix} \end{cases} \tag{14}$$

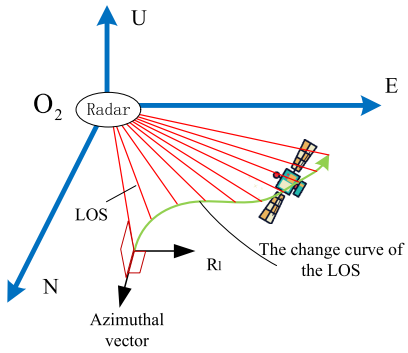

Fig. 4. Variation curve of the LOS.

where t_k is the intermediate time of the kth subaperture, and $\dot{\theta}(t_k)$ and $\dot{\varphi}(t_k)$ are the first-order derivatives of $\theta(t_k)$ and $\varphi(t_k)$, respectively. Then, the scatterers of the space target project on the kth image plane can be represented as

$$\hat{P}_k = \Gamma_k \cdot \mathbf{p}_{0n} \tag{15}$$

where $\hat{P}_k$ is the coordinate of the projection scatterers on the kth image plane, and Γ_k denotes the projection matrix, which can be expressed as

$$\Gamma_k = [r_k, f_{a,k}]^T. \tag{16}$$

III. Three-Dimensional Geometry Reconstruction With Vote Scoring

As discussed in Section II, the long-time echoes should be divided into overlapped subapertures. Based on [34] and [35], we can obtain high-resolution ISAR image sequences. From these subimages, we need to select those with less clutter, obtaining more target information, and good focus for further processing. Due to the differences in target pose relative to radar, there may be rotation, scaling, and other phenomena among the subimages, which can be corrected through image matching. After correction, scatterers are extracted from the images and associated based on voting accumulation. The associated scatterers are then filtered and backprojected to achieve a 3-D reconstruction of the target. The overall process is illustrated in Fig. 5.

A. Conversion of Images With Different Subapertures

After splitting, we can obtain the overlapped subapertures. The high-resolution ISAR image sequences can be obtained with imaging processing [34], [35], such as keystone and autofocus. However, these algorithms also introduce random phases, resulting in a random translation of the ISAR image for each subaperture. Therefore, image correlation of the sequential ISAR is necessary before trajectory association. Moreover, the overlapped subapertures result in redundant information. Therefore, to improve the processing accuracy and speed, the image with fewer stray points and good focus should be selected. In addition, such image distribution should cover all views as evenly as possible.

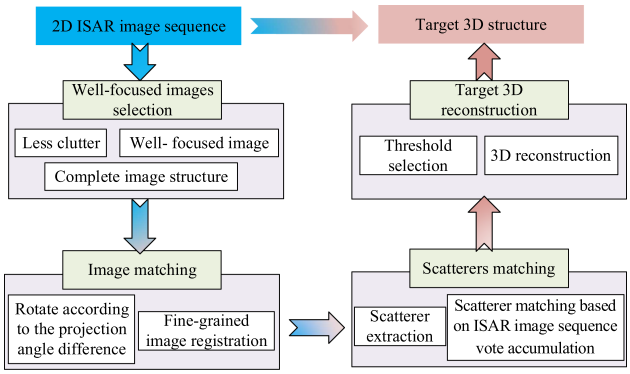

Fig. 5. Overall flowchart of the proposed 3-D reconstruction algorithm.

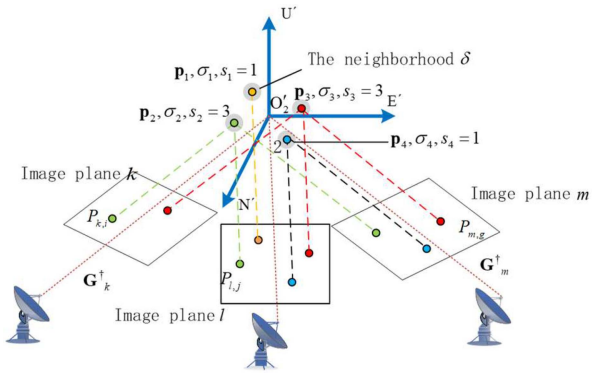

Fig. 6. Schematic diagram of the SISVA.

After selection, the selected ISAR image should be transformed into a scatterer set via scatterer center extraction. There are two commonly used methods to extract the scattering center, namely the orthogonal matching pursuit method and the peak extraction method. The total number of selected ISAR images is assumed to be K. After signal processing, the image from kth subaperture can be expressed as

$$I_k(r, f_a; t_k) = \sum_{n=1}^{N} \sigma_{k,n} \mathrm{sinc}\left(\frac{2B}{C}(r - r_k \cdot p_n - \Delta r_k)\right) \cdot \mathrm{sinc}\left(\frac{1}{PRF}(f_a - f_{a,k} \cdot p_n - \Delta f_{a,k})\right) \tag{17}$$

where Δr_k and $\Delta f_{a,k}$ represent the image displacements caused by phase compensation in the kth subaperture. After scatterers extraction, the scatterers set can be represented as

$$\hat{S}_k = \begin{bmatrix} \hat{r}_{k,1} \cdots \hat{r}_{k,n} \cdots \hat{r}_{k,N} \\ \hat{f}_{a,k,1} \cdots \hat{f}_{a,k,n} \cdots \hat{f}_{a,k,N} \end{bmatrix}, \quad k = 1, 2, \ldots, K \tag{18}$$

where

$$\begin{cases} \hat{r}_{k,n} = r_k \cdot p_n + \Delta r_k \\ \hat{f}_{a,k,n} = f_{a,k} \cdot p_n + \Delta f_{a,k} \end{cases}, \quad n = 1, 2, \ldots, N. \tag{19}$$

By combining (14)–(16), we can conclude that the scatterer position of the kth subaperture should be

$$\hat{S}_k = \Gamma_k \cdot \mathbf{p}_{0n} + [\Delta r_k, \Delta f_{a,k}]^T. \tag{20}$$

It follows that the projection of the scatterer of the kth image onto the gth image can be expressed as

$$\hat{S}_{k|g} = \Gamma_g \cdot {\Gamma_k}^{\dagger} \cdot \hat{S}_k + [\Delta r_g, \Delta f_{a,g}]^T - \Gamma_g \cdot {\Gamma_k}^{\dagger} \cdot [\Delta r_k, \Delta f_{a,k}]^T \tag{21}$$

where $[\cdot]^{\dagger}$ denotes the pseudoinverses of the matrix. Δr_g and $\Delta f_{a,g}$ represent the image displacements caused by phase compensation in the gth subaperture.

B. Scatterer Sets Matching by ISAR Image Sequence Vote Accumulation

After the image registration in Section III-A, it is possible to obtain a general relation for the set of scatterers of two adjacent images. In this section, to implement multiple subapertures matching, the anisotropy of electromagnetic scattering and the occlusion between different scatterers should be considered. As a result, some scatterers may be detected in several consecutive images. The alternative case is when the extracted scatterer is composed of noise, which can only be detected in one or two images. Therefore, it would have a considerably smaller score than that of the true scatterer vote accumulation.

Motivated by this idea, we propose an original technique for 3-D reconstruction by using a scatterer from ISAR image sequence vote accumulation (SISVA). First, we project the 2-D sequential scatterer set into a 3-D space for processing. If multiple sequential scatterers are projected onto the same spatial position, the scatterer score increases. If there are no close scatterers, it is considered that there is no match. Unmatched scatterers are also added to the set of scatterers as a new reference for matching. Finally, 3-D reconstructions can be obtained from high-scoring scatterers. The detailed procedure is shown in Fig. 6.

For example, $\mathbf{p}_2, \sigma_2, s_2 = 3$, $\mathbf{p}_2$ means that the spatial position of the second scatterer of the target and the energy history is σ_2. $s_2 = 3$ means that three subapertures are visible, and the index of their associated subviews is recorded. Suppose K represents the number of 2-D scatterer sets, SISVA can be outlined as follows.

Step 1. Initialization. Let $k = 2$, the reference scatterer set $S_{\text{base}} = S_1$, where S_1 is the scatterer set of the first subaperture. The reference scatterer set is intended to be aligned with the kth image scatterer set, and it will dynamically expand during the matching process. In initial some variations, $Mr = [v, c]^T$, where v denotes the index of subaperture, and c denotes the index of scatterer in the vth subaperture. Initialize the score set s and Mr as follows:

$$\begin{cases} s_{\text{base}} = [1 \quad 1 \quad \ldots \quad 1]_{1 \times M} \\ Mr_{\text{base}} = \left\{[v, 1]^T, [v, 2]^T, \ldots, [v, M]^T\right\} \\ v = 1 \end{cases} \tag{22}$$

where M is the number of scatterers in S_{base}, and $\{\cdot\}^T$ denotes the transpose of matrix.

Step 2. Scatterer matching. To align the reference scatterer set S_{base} with the scatterer set S_k from the kth image, we correct

S_k to form S_{kc}. Subsequently, we perform matching between S_{base} and S_{kc}. For each successfully matched scatterer in S_{base}, we increment its score by 1, update score and matched pairs as

$$\begin{cases} s_{\text{base}}(\text{match}_{\text{base}}) = s_{\text{base}}(\text{match}_{\text{base}}) + 1 \\ Mr_{\text{base}}\{\text{match}_{\text{base}}\} = \left[Mr_{\text{base}}\{\text{match}_{\text{base}}\}; [k, \text{match}_k]^T\right] \end{cases} \tag{23}$$

where $\text{match}_{\text{base}}$ is the index of successfully matched scatterer in S_{base}, and match_k is the index of successfully matched scatterer in S_k. The elements of $S_{\text{base}}(\text{match}_{\text{base}})$ and $S_k(\text{match}_k)$ have a one-to-one correspondence.

Step 3. 3-D reconstruction. Based on the matched scatterers, 3-D reconstruction with the least square method can be achieved by

$$\mathbf{U}_{\text{3-D}} = \left(\Gamma_{\text{base},k}^T \Gamma_{\text{base},k}\right)^{-1} \Gamma_{\text{base},k}^T S_c \tag{24}$$

$$\Gamma_{\text{base},k} = \begin{bmatrix} \Gamma_{\text{base}} \\ \Gamma_k \end{bmatrix}_{4\times 3} \tag{25}$$

where Γ_{base} and Γ_k are the projection matrices of the reference scatterer set and the kth subaperture, $\mathbf{U}_{\text{3-D}}$ is the 3-D position, and S_c represents the matrix composed of matched scatterers. Assuming that N scattering points are successfully matched, S_c is represented as

$$S_c = \begin{bmatrix} S_{\text{base}}(\text{match}_{\text{base}}(1)) & \cdots\cdots & S_{\text{base}}(\text{match}_{\text{base}}(N)) \\ S_k(\text{match}_k(1)) & \cdots\cdots & S_k(\text{match}_k(N)) \end{bmatrix}_{4\times N}. \tag{26}$$

Step 4. Update the matched scatterer set. The 3-D scatterers $\mathbf{U}_{\text{3-D}}$ are projected onto the kth subaperture to obtain the reconstruction scatterers S_{match} in the kth subaperture

$$S_{\text{match}} = \Gamma_k \mathbf{U}_{3-\text{D}}. \tag{27}$$

Step 5. Update the reference scatterer set. For the matched scatterers in S_{base}, let $S_{\text{base}}(\text{match}_{\text{base}}) = S_{\text{match}}$. Let mis_{base} denotes the index of mismatched scatterers in S_{base}, then

$$S_{\text{base}}(\text{mis}_{\text{base}}) = \Gamma_k {\Gamma_{\text{base}}}^{-1} S_{\text{base}}(\text{mis}_{\text{base}}). \tag{28}$$

Suppose mis_k denotes the index of mismatched scatterers in S_k, the total mis_k is L, then

$$\begin{cases} s_{\text{base}} = \left[s_{\text{base}}, [1, 1, \ldots, 1]_{1\times L}\right] \\ Mr_{\text{base}} = \Big\{Mr_{\text{base}}, [k, \text{mis}_k(1)]^T, \\ \qquad [k, \text{mis}_k(2)]^T, \ldots, [k, \text{mis}_k(L)]^T\Big\} \\ S_{\text{base}} = [S_{\text{base}}, S_k(\text{mis}_k(1)), \\ \qquad S_k(\text{mis}_k(2)), \ldots, S_k(\text{mis}_k(L))] \\ \Gamma_{\text{base}} = \Gamma_k. \end{cases} \tag{29}$$

Finally, update $k = k + 1$.

Step 6. Update $k = k + 1$, repeat step 2 to step 4 until $k > K$, and the score matrix s_{base} and scatterer matching chain Mr_{base} can be obtained.

After obtaining the scatterer matching chain, the true and false scatterers can be distinguished based on the score of the matching chain and the scatterer energy. A chain satisfying the threshold condition is a true scatterer.

C. Analysis of 3-D Reconstruction Based on SISVA

In the scatterer matching procedure, all possible combinations are matched. Therefore, in this section, we set a minimum score threshold and reconstruct the scatterers with scores greater than this threshold. Finally, all reconstruction results are integrated to obtain the target 3-D reconstructed set of scatterers.

Assume that the projection matrix and projection position of K images are known, then the nth 3-D scatterers can be obtained by

$$\mathbf{p}_n = \left(\Gamma^T\Gamma\right)^{-1}\Gamma^T\mathbf{s}_n \tag{30}$$

where $\mathbf{s}_n$ denotes the matched 2-D scatterers position, $\mathbf{p}_n$ is the 3-D scatterers' positions, and Γ is the projection matrix, represented as $\Gamma = [\Gamma_1, \Gamma_2, \Gamma_3, \ldots, \Gamma_K]^T{}_{2K\times 3}$.

After SISVA, there are $\sum_{k=2}^{K} C_K^k$ combinations, and k is the scoring time. The greater the scoring times, the more matched images of the corresponding combination. Let the minimum score threshold be K_t, then all match combinations with scores less than K_t will be discarded. In general, raising the score threshold results in a reduction in the number of clutterers within the reconstructed outcome. However, it compromises the structural integrity. Conversely, lowering the threshold enhances structural integrity but enhances the occurrence of clutterers.

D. Performance Evaluation Method

To better evaluate the quality of a 3-D reconstruction algorithm, we believe that there are three main criteria: first, the widely recognized root-mean-square error (RMSE), which represents the accuracy of the reconstruction; second, we have devised the false positive ratio (FPR) and the false negative ratio (FNR) to reflect the proportion of scatterers that do not belong to the target after 3-D reconstruction and the probability of missing real scatterers, respectively. A high number of reconstructed scatterers does not necessarily indicate a low number of estimated real scatterers, and vice-versa. Therefore, while FPR and FNR may seem conflicting, they cannot replace each other.

1) Root-Mean-Square Error: The RMSE is defined as

$$E_{\text{RMSE}} = \sqrt{\frac{1}{N}\sum_{n=1}^{N}\left(\mathbf{p}_n^{\text{opt}} - \mathbf{p}_n\right)^2}. \tag{31}$$

When the true positions of the scatterers are known, we can assess the performance of the algorithm by calculating the RMSE, where N denotes the number of scatterers on the target, $\mathbf{p}_n^{\text{opt}}$ represents the 3-D coordinated of the nth reconstructed scatterer, and $\mathbf{p}_n$ is the real 3-D position of the nth scatterer. RMSE is the accurate criterion for a simple target with a few scatterers. However, when the true positions of the scatterers are unavailable, we can utilize the RMSE to evaluate the consistency between the inverted target size and the actual target size, thereby indirectly assessing the accuracy of the proposed algorithm. In

TABLE I
RADAR SYSTEM PARAMETERS

Radar location	107.4E, 41.68N, 6371 Km	
Radar system parameters	Center frequency	10 GHz
	Pulse repetition frequency	300 Hz
	Sample frequency	20 MHz
	Bandwidth	1 GHz
	Relative rotation angle	134.7°
	Azimuth resolution	Changing with subview
	Range resolution	0.15 m

this case, $\mathbf{p}_n^{\text{opt}}$ represents the estimated size of the target. $\mathbf{p}_n$ denotes the real size of the target, and N denotes the number of size parameters.

2) False Positive Ratio: For 3-D reconstruction, the accuracy of the reconstructed scatterer is important. Meanwhile, it is also important that the reconstructed scatterers belong to the true scatterers of the target. The 3-D reconstruction can also be viewed as a binary hypothesis detection problem, depending on whether the reconstructed scatterer is the true scatterer or not. Thus, the FPR can be expressed as

$$P_{\text{FPR}} = P\left(H_0 \,|(H_0 + H_1)\right) \tag{32}$$

where H_1 denotes the real scatterer, and H_0 denotes the noise and clutter. Therefore, P_{FPR} denotes the ratio of false scatterers in all the reconstructed scatterers. The higher the FPR, the more chaotic the reconstructed 3-D structure.

3) False Negative Ratio: The evaluation of the 3-D reconstruction performance can also be based on the true scatterers obtained by the reconstruction less than the number of target real scatterers. Thus, the FNR can be expressed as

$$P_{\text{FNR}} = P\left((H_2 - H_1)\,|H_2\right) \tag{33}$$

where H_2 denotes the real scatterers, and H_1 denotes the estimated true scatterers. If the estimated true scatterer falls short of its real scatterers associated with the target, it indicates that the reconstructed structure fails to accurately capture the full essence of the true target structure.

IV. EXPERIMENTAL ANALYSIS

A. Experiment Based on a Simple Point Model

It is widely acknowledged that the number of subviews and SNR play crucial roles in influencing the 3-D reconstruction process. To investigate the impact of each factor on the 3-D reconstruction algorithm, a series of comparison experiments were conducted on a simulated scatterer model consisting of 20 scatterers. Table I provides the introduction of the radar system parameters. The simulated radar is located at (107.4E, 41.68N, 6371 km) and works at *X*-band. The transmitted signal bandwidth is 1 GHz. The variation of pitch and azimuthal angles is shown in Fig. 7. In the simulation, we received 7560 echoes total and divided them into 48 subapertures. The total relative rotation angle is 134.7°. Subsequently, the radar echo is divided into multiple subviews every 3.5°. Therefore, the pulse number of subview changes with the relative rotation angle.

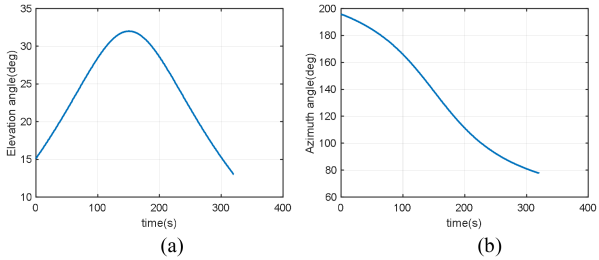

(a) (b)

Fig. 7. Variation of pitch and azimuthal angle for simulation. (a) Variation of pitch. (b) Variation of azimuth.

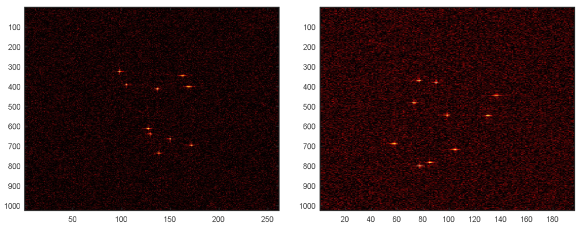
(a) (b)

Fig. 8. Partial ISAR image results with SNR $= -10$ dB. (a) 1st ISAR image. (b) 20th ISAR image.

In this simulation, the SNR is -10 dB, achieved by utilizing the awgn function in MATLAB to add noise to the radar image, obtaining high-quality ISAR images using existing algorithms. Partial ISAR image sequence is shown in Fig. 8(a) and (b), which are the results of the 1st and 20th frames, respectively.

According to the radar measurement information, the projection vectors of each subaperture can be obtained. Then, the proposed method is performed on the image sequence. The 3-D reconstruction results based on MFA, ISEA, and SISVA are presented in Fig. 9(a)–(c), respectively. Fig. 9 shows the comparison between the reconstructed scatterers and the real ones. The black points denote the reconstructed scatterers, and the red circles represent the real ones. To better evaluate the 3-D reconstruction methods, we can compute the RMSE, which is 0.96 m, 0.24 m, and 0.21 m, respectively. Although the ISEA achieves the accurate 3-D reconstruction, it often results in a higher number of spurious points due to factors, such as noise and sidelobes.

B. Experiment Based on a Complex Point Model

In this section, we need to conduct simulation experiments on more complex targets to verify the practical performance of the algorithm. The experimental conditions are consistent with Section IV-A. Fig. 10 depicts the 3-D reconstruction results obtained from ten subviews using three different algorithms at an SNR of 10 dB. Upon examination of the three orthogonal views, it becomes evident that the ISEA algorithm produces numerous spurious points in the reconstructed 3-D structure.

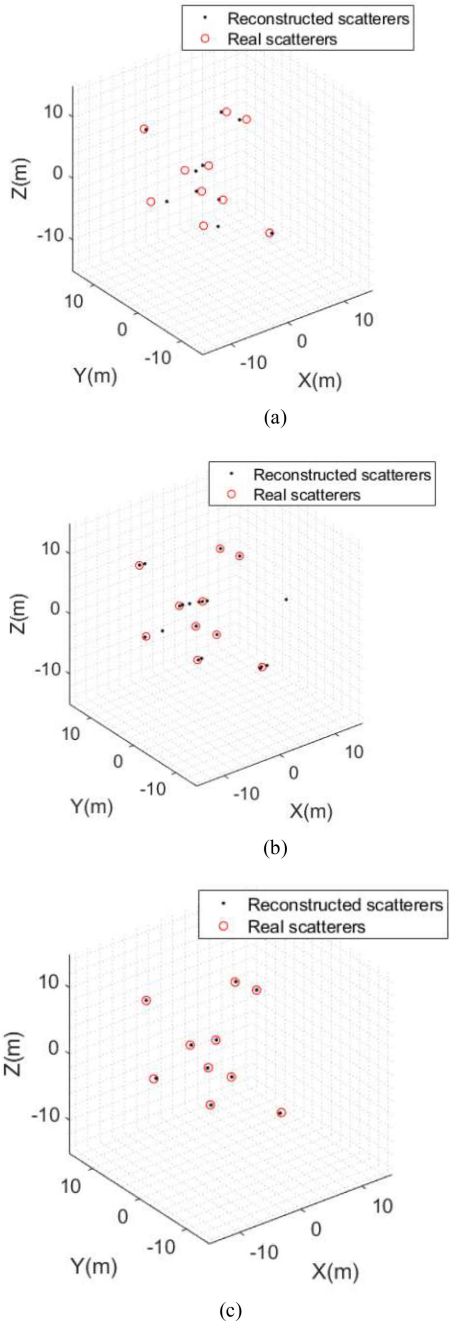

Fig. 9. Results of 3-D reconstruction of 20 scatterers according to different methods with SNR $= -10$ dB. (a) Three-dimensional results based on MFA. (b) Three-dimensional results based on ISEA. (d) Three-dimensional results based on SISVA.

To demonstrate the performance of these 3-D reconstruction algorithms more comprehensively, we conduct 50 Monte Carlo experiments with different perspectives and different SNRs. Fig. 11 shows the 3-D reconstruction results for 50 Monte Carlo experiments with different numbers of perspectives. After observation, we can find that the 3-D reconstruction performance of MFA exhibits significant fluctuations as the number of perspectives varies. Meanwhile, SISVA and ISEA gradually improve their metrics as the number of perspectives increases. As observed in Fig. 11(a), SISVA and ISEA both achieve high accuracy in scatterer estimation, with SISVA having slightly better estimation accuracy than ISEA.

An additional observation of Fig. 11(b) and (c) reveals that, although ISEA performs better in terms of FNR, with an accuracy of approximately 0.22, SISVAs FNR exceeds 0.42. However, ISEA has a higher FPR of approximately 0.39, while SISVA has an FPR of approximately 0.13.

Fig. 12 shows the results of 50 Monte Carlo experiments with different SNRs. The performance of MFA-based 3-D reconstruction gradually improves in three metrics. This indicates that the performance of 3-D reconstruction gradually improves with increasing SNR.

Compared with MFA, the ISEA algorithm performs robustly on all three metrics, is not affected by SNR, and has higher accuracy than MFA with the lowest FNP but more ghosting. As for the proposed SISVA algorithm, its performance at -5 dB is not excellent. However, when the SNR is above -5 dB, all three metrics are essentially unaffected by the SNR. The accuracy is slightly better than the ISEA algorithm and the ghost rate is significantly lower. Figs. 11(c) and 12(c) reveal that the proposed method does not perform well as ISEA. This can be attributed to several factors inherent in the proposed methodology.

First, the proposed method involves the extraction and trajectory association of scatterers. However, when dealing with dense scatterer models, the projection process can suffer from insufficient resolution. This leads to an inability to distinguish between closely spaced scatterers, resulting in fewer scatterers reconstructed.

Second, the proposed method has a higher threshold for recognizing and reconstructing scattering points. It requires a certain number of subviews for a scatterer to be considered real and reconstructed in three dimensions. In contrast, ISEA, which relies on energy accumulation, is more adept at reconstructing low-energy scattering points that appear in only a few subviews. This is also the reason why ISEA has a high FPR.

Consequently, the FNR metric for the proposed method is higher than that of the ISEA algorithm. While this metric may not demonstrate the superiority of the proposed algorithm in this particular aspect, it nonetheless provides a comprehensive assessment of the overall performance of the 3-D reconstruction algorithm.

On the other hand, SISVA and ISEA share a similarity in which they do not require the reconstructed scatterers to be present in all perspectives. In other words, they do not require continuity of scatterer trajectories, which is a requirement of MFA. Since ISEA cannot determine which perspective each scatter comes from, it cannot assess the effect of a change in the minimum number of matched perspectives when the total number of perspectives remains constant. However, SISVA can achieve this. The following 50 Monte Carlo experiments are conducted for the minimum matching number ranging from 3 to 25, and the experimental results are presented in Fig. 13, which shows the results of how the 3-D reconstruction performance of the SISVA algorithm varies with the minimum number of matched perspectives, for a total of 25 perspectives with an SNR of 10 dB. In this experiment, the actual number of scatterers

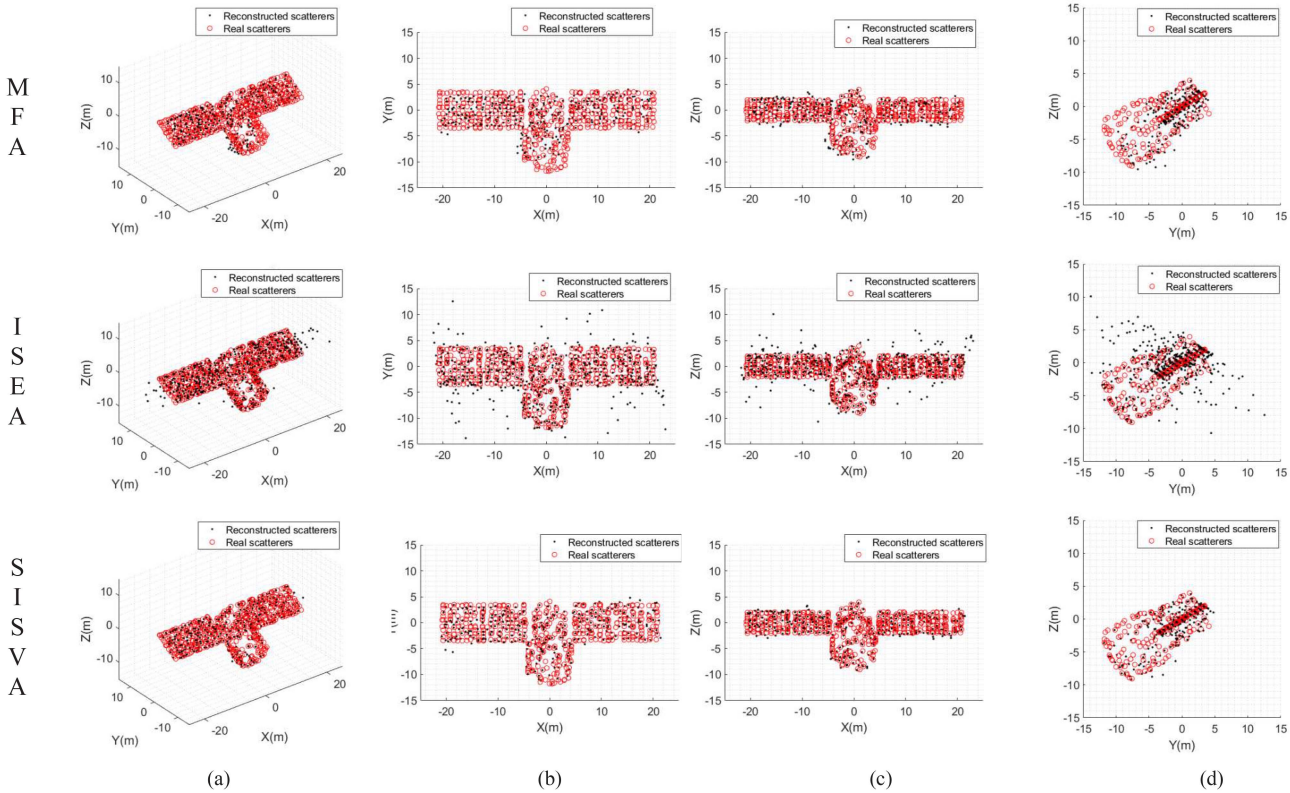

Fig. 10. Performance evaluation of three 3-D reconstruction algorithms with varying SNR with 11 viewing angles. (a) Results of RMSE. (b) Results of FPR. (c) Results of FNR.

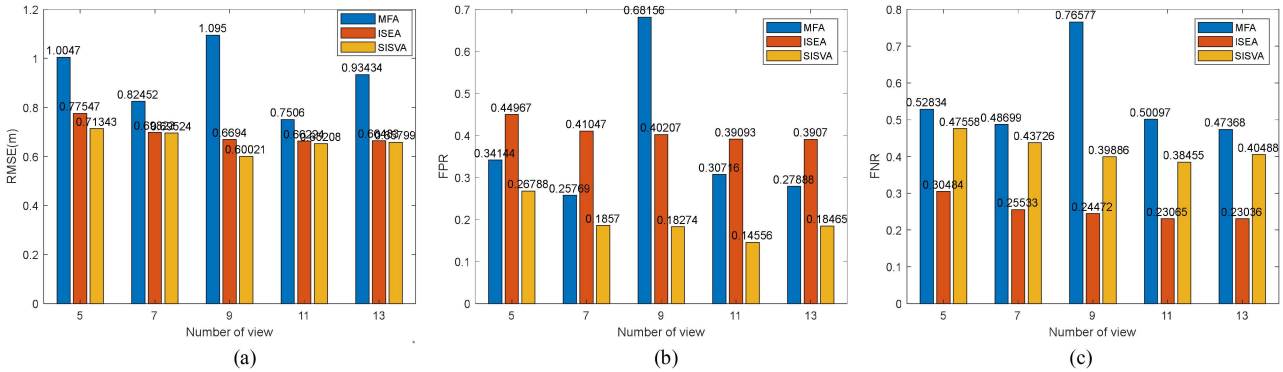

Fig. 11. Performance evaluation of three 3-D reconstruction algorithms with varying perspectives when SNR is 10 dB. (a) Results of RMSE. (b) Results of FPR. (c) Results of FNR.

on the target is 475. As can be seen in Fig. 13(a), with the change in the minimum number of matching perspectives, the number of scatterers obtained through SISVA exhibits a trend of rapid decline followed by slow decline. At least, 3 of the 25 perspectives need to be matched to obtain approximately 600 scatterers, which is reduced to approximately 270 scatterers when the number of perspectives is up to 25. Fig. 13(b) shows the 3-D reconstruction accuracy, RMSE, which is approximately 0.7 m, then gradually decreases to approximately 0.61 m. In Fig. 13(c), the black solid line represents FNR, while the red dashed line represents FPR. As shown in Fig. 13(c), with the increase in the minimum number of matching perspectives for scatterers, SISVAs FPR rapidly decreases, while FNR rapidly increases. When the minimum number of matched perspectives for scatterers is approximately 7, the FPR and FNR of SISVA are equal and both are approximately 0.3. This means that approximately 30% of the true scatterers are not reconstructed in 3-D. At the same time, approximately 30% of the reconstructed scatterers do not correspond to the true scatterers, which is considered a “ghost” phenomenon.

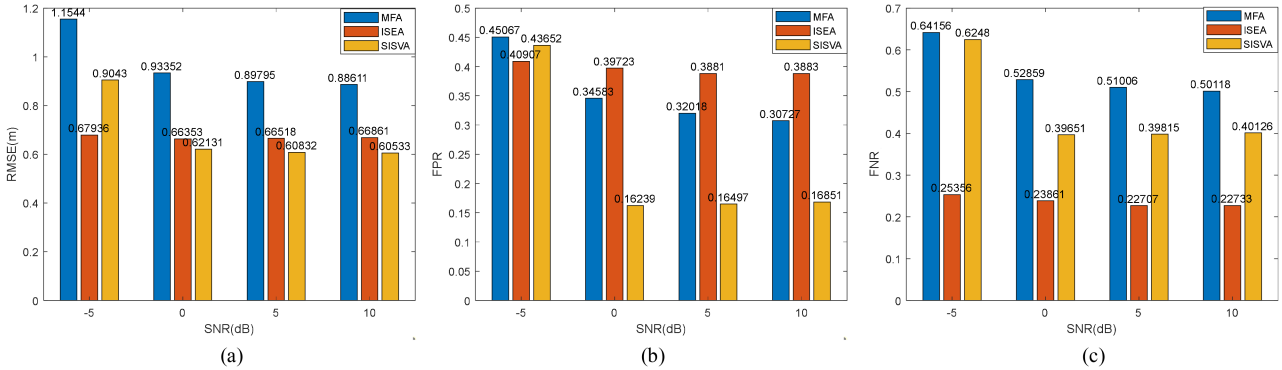

Fig. 12. Performance evaluation of three 3-D reconstruction algorithms with varying SNR with 11 viewing angles. (a) Results of RMSE. (b) Results of FPR. (c) Results of FNR.

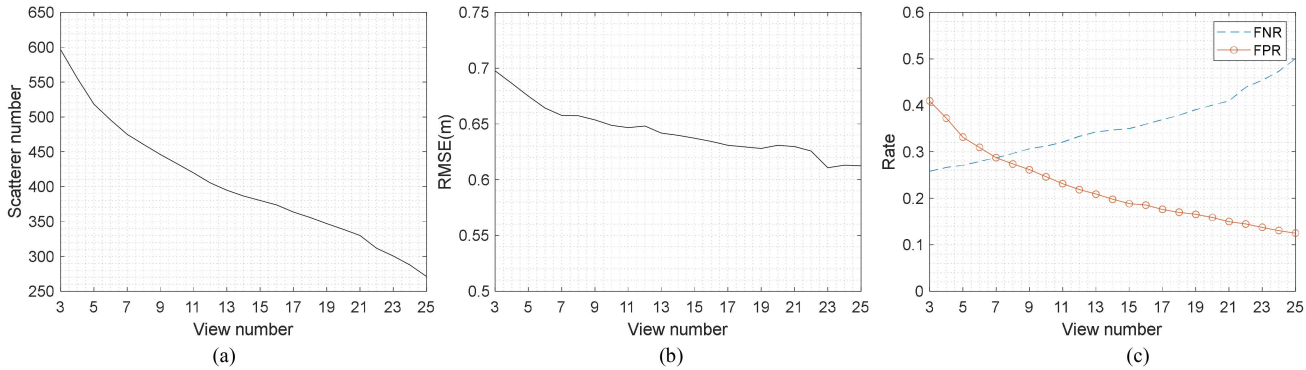

Fig. 13. When considering a total of 25 perspectives with an SNR of 10 dB, the 3-D reconstruction performance of the SISVA algorithm varies with the minimum number of matched perspectives. (a) Number of scatterers reconstructed. (b) Results of RMSE. (c) Results of FPR and FNR.

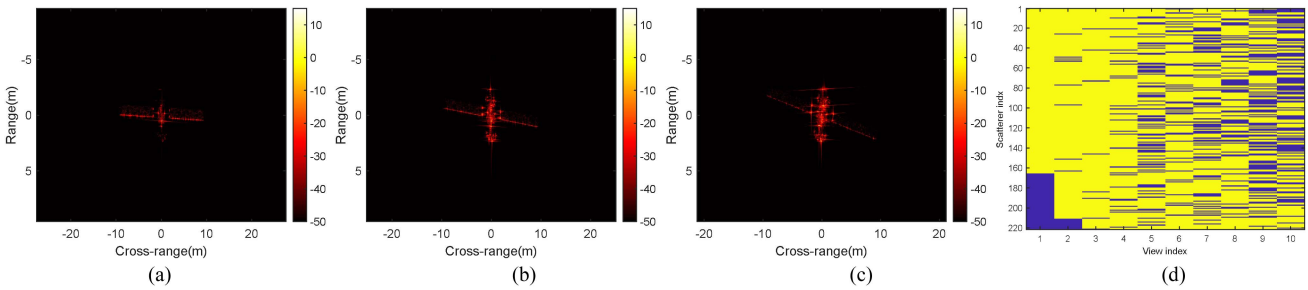

Fig. 14. Partial ISAR image results and the obtained trajectory of the third experiment. (a) 1st ISAR image. (b) 3rd ISAR image. (c) 13th ISAR image. (d) Obtained trajectory of scatterers.

C. *Experiment Based on an Electromagnetic Simulation*

To show the effect of the algorithm more effectively, we carry out electromagnetic simulation experiments on the electromagnetic satellite simulation. The radar parameters in this experiment are the same as in Section IV-A. In this experiment, ten discontinuous subapertures are used to reconstruct the object in three dimensions. Fig. 14 shows some of the ISAR imaging results obtained with the PFA processing. It can be seen from Fig. 14(d) that most scatterers cannot be matched in all perspectives. Fig. 15(a) is the model used in the experiment. Fig. 15(b) shows the 3-D reconstruction results obtained by the MFA method. Due to the full trajectory requirement of MFA, many noncontinuous scatterer trajectories are linearly interpolated to obtain the full trajectory. Because of the requirement for scattering points to appear and be associated across essentially all subviews, the 3-D reconstruction obtained by MFA results in fewer scatterers. Fig. 15(c) shows the 3-D reconstruction result generated by the ISEA method, which evidently has many false points. Fig. 15(d) shows the 3-D structure obtained by SISVA method, with a clear target structure and fewer outliers.

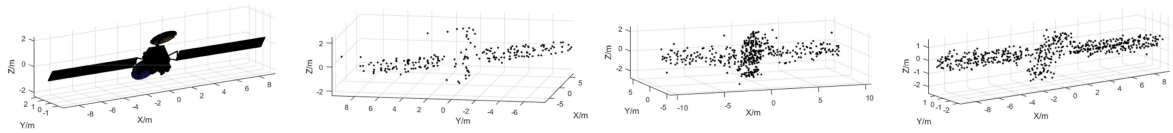

(a) (b) (c) (d)

Fig. 15. Three-dimensional reconstruction results of three 3-D reconstruction algorithms. (a) Target model. (b) Three-dimensional results based on MFA. (c) Three-dimensional results based on ISEA. (d) Three-dimensional results based on SISVA.

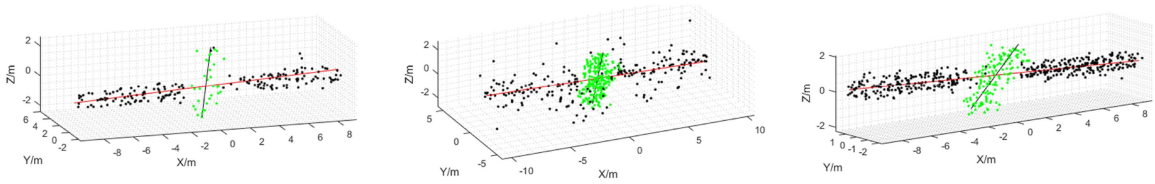

(a) (b) (c)

Fig. 16. Extract the central axis of the solar panel and the main body. (a) Extract based on MFA. (b) Extract based on ISEA. (c) Extract based on SISVA.

TABLE II
LENGTH ESTIMATION OF SOLAR PANEL AND MAIN BODY

Items	Target model	MFA	ISEA	SISVA
Length of solar panel/m	18.86	19.12	18.83	18.89
Length of the main body/m	6.18	5.25	5.92	5.94
Error of solar panel/m		0.26	0.03	0.03
Error of the main body/m		0.93	0.26	0.24

As the real scatterers are unavailable, to evaluate the accuracy of the 3-D reconstruction algorithm, we conduct component segmentation on the satellite 3-D reconstruction. The results of the measurements and analysis are presented in Fig. 16 and Table II. In Fig. 16, black dots represent the segmented solar panels, while green dots indicate the main body of the satellite. The red line signifies the extracted central axis of the solar panels, and the black line represents the extracted central axis of the satellite's main body. The lengths of the extracted central axes for each component are presented in Table II, indicating that both SISVA and ISEA achieve comparable accuracy and significantly outperform MFA.

V. SUMMARY AND ANALYSIS

In this article, we propose a 3-D reconstruction method utilizing a single antenna to yield a sequence of radar images. The performance of the three 3-D reconstruction algorithms is thoroughly examined under various perspectives and SNRs. Depending on the practical considerations and specific conditions, a suitable 3-D reconstruction algorithm can be flexibly chosen. During the experiment, it was observed that the 3-D structure of the target obtained by MFA has arbitrary orientations. Therefore, in this study, the orientation correction is applied to all the 3-D reconstruction results obtained through MFA to align them with the actual orientation of the target for more accurate performance evaluation. Besides, the MFA algorithm requires continuous scatterer trajectories, a criterion that is often challenging to fulfill in practical applications. To address this, we predict the missing trajectories to satisfy the requirements of the MFA algorithm. However, MFA has stringent requirements on the accuracy of the scatterer trajectory association. The imprecise scatterer trajectories can occasionally cause the 3-D reconstruction to fail, resulting in complex 3-D positions obtained by matrix factorization. Therefore, such cases are excluded from the experimental performance evaluation.

In Section IV, the 3-D structure of the target obtained with ISEA and SISVA is shown to be aligned with the original target pose through experimental results. Meanwhile, the RMSE accuracy of ISEA and SISVA is relatively close to and higher than that of MFA. ISEA often leads to a large number of stray points due to the selection of energy accumulation thresholds and the application of 3-D space division strategies. In contrast, this article employs a voting accumulation method that effectively reduces the generation of stray points through the extraction and association of scatterers. This is because scatterers caused by noise rarely appear in the same position from multiple subperspectives. Therefore, the accumulated votes for noise are fewer, while the number of votes for real scatterers is higher. Additionally, since the method presented in this article does not require 3-D space division, it offers a reduced computational load compared with the ISEA.

VI. CONCLUSION

For the three-axis stabilized space targets, high-resolution 2-D image sequences of the target can be obtained through multiple observations. Since the attitude of the space target

remains stationary in the orbital coordinate system, the relative motion is primarily generated by changes in the radar range. Therefore, a method is proposed to reconstruct the 3-D geometric structure of the target using voting and scoring based on the correlation results of specific points in sequential ISAR images at multiple perspectives. Unlike MFA, this method does not require continuous scatterer trajectory association and the 3-D reconstruction is aligned with the actual target pose with higher accuracy. Compared with ISEA, this algorithm has a lower FPR and higher reliability. The experimental results based on the simulated data demonstrate the effectiveness and robustness of the proposed method. However, the proposed method is not suitable for targets with low SNR due to the inability to obtain scatterers for matching between the two perspectives, which limits the performance of the proposed method. Our future work will focus on these issues.

REFERENCES

[1] C.-C. Chen and H. C. Andrews, "Target-motion-induced radar imaging," *IEEE Trans. Aerosp. Electron. Syst.*, vol. AES-16, no. 1, pp. 2–14, Jan. 1980.

[2] X. Lv, M. Xing, C. Wan, and S. Zhang, "ISAR imaging of maneuvering targets based on the range centroid Doppler technique," *IEEE Trans. Image Process.*, vol. 19, no. 1, pp. 141–153, Jan. 2010.

[3] D.-W. Wang, X.-Y. Ma, A.-L. Chen, and Y. Su, "High-resolution imaging using a wideband MIMO radar system with two distributed arrays," *IEEE Trans. Image Process.*, vol. 19, no. 5, pp. 1280–1289, May 2010.

[4] Q. Zhang, T. S. Yeo, and G. Du, "ISAR imaging in strong ground clutter using a new stepped-frequency signal format," *IEEE Trans. Geosci. Remote Sens.*, vol. 41, no. 5, pp. 948–952, May 2003.

[5] D. Kucharski et al., "Attitude and spin period of space debris ENVISAT measured by satellite laser ranging," *IEEE Trans. Geosci. Remote Sens.*, vol. 52, no. 12, pp. 7651–7657, Dec. 2014.

[6] G. Xu, B. Zhang, J. Chen, and W. Hong, "Structured low-rank and sparse method for ISAR imaging with 2-D compressive sampling," *IEEE Trans. Geosci. Remote Sens.*, vol. 60, Nov. 2022, Art. no. 5239014.

[7] S. D'Amico, M. Benn, and J. L. Jorgensen, "Pose estimation of an uncooperative spacecraft from actual space imagery," *Int. J. Space Sci. Eng.*, vol. 2, no. 2, pp. 171–189, 2014.

[8] N. Bobrinsky and L. Del Monte, "The space situational awareness program of the European space agency," *Cosmic Res.*, vol. 48, no. 5, pp. 392–398, 2010.

[9] K. Demars, "Nonlinear orbit uncertainty prediction and rectification for space situational awareness," Ph.D. dissertation, Dept. Aerosp. Eng. Eng. Mech., Univ. Texas Austin, Austin, TX, USA, 2010.

[10] B. Zhang, G. Xu, H. Yu, H. Wang, H. Pei, and W. Hong, "Array 3-D SAR tomography using robust gridless compressed sensing," *IEEE Trans. Geosci. Remote Sens.*, vol. 61, Mar. 2023, Art. no. 5205013, doi: 10.1109/TGRS.2023.3259980.

[11] J. Zhou, Z. Shi, and Q. Fu, "Three-dimensional scattering center extraction based on wide aperture data at a single elevation," *IEEE Trans. Geosci. Remote Sens.*, vol. 53, no. 3, pp. 1638–1655, Mar. 2015.

[12] G. Wang, X.-G. Xia, and V. C. Chen, "Three-dimensional ISAR imaging of maneuvering targets using three receivers," *IEEE Trans. Image Process.*, vol. 10, no. 3, pp. 436–447, Mar. 2001.

[13] M. Martorella, F. Salvetti, and D. Staglianò, "3D target reconstruction by means of 2D-ISAR imaging and interferometry," in *Proc. IEEE Radar Conf.*, 2013, pp. 1–6.

[14] X. Xu and R. M. Narayanan, "Three-dimensional interferometric ISAR imaging for target scattering diagnosis and modeling," *IEEE Trans. Image Process.*, vol. 10, no. 7, pp. 1094–1102, Jul. 2001.

[15] C. Ma, T. S. Yeo, Q. Zhang, H. S. Tan, and J. Wang, "Three-dimensional ISAR imaging based on antenna array," *IEEE Trans. Geosci. Remote Sens.*, vol. 46, no. 2, pp. 504–515, Feb. 2008.

[16] Z. Wang, Q. Guo, X. Tian, T. Chang, and H.-L. Cui, "Near-field 3-D millimeter-wave imaging using MIMO RMA with range compensation," *IEEE Trans. Microw. Theory Techn.*, vol. 67, no. 3, pp. 1157–1166, Mar. 2019.

[17] M. E. Yanik and M. Torlak, "Near-field MIMO-SAR millimeter-wave imaging with sparsely sampled aperture data," *IEEE Access*, vol. 7, pp. 31801–31819, 2019.

[18] Y. Guo, Y. Li, and Y. Zhang, "Research on MIMO-ISAR high resolution imaging technology," in *Proc. IEEE 4th Adv. Inf. Manage., Communicates, Electron. Autom. Control Conf.*, 2021, pp. 169–174.

[19] J. S. Seybold and S. J. Bishop, "Three-dimensional ISAR imaging using a conventional high-range resolution radar," in *Proc. IEEE Nat. Radar Conf.*, 1996, pp. 309–314.

[20] M. A. Stuff, P. Sanchez, and M. Biancalana, "Extraction of three-dimensional motion and geometric invariants from range dependent signals," *Multidimensional Syst. Signal Process.*, vol. 14, pp. 161–181, Jan. 2003.

[21] Y. Zhou, L. Zhang, C. Xing, P. Xie, and Y. Cao, "Target three-dimensional reconstruction from the multi-view radar image sequence," *IEEE Access*, vol. 7, pp. 36722–36735, 2019.

[22] D. Xu, M. Xing, X.-G. Xia, G.-C. Sun, J. Fu, and T. Su, "A multi-perspective 3D reconstruction method with single perspective instantaneous target attitude estimation," *Remote Sens.*, vol. 11, no. 11, 2019, Art. no. 1277, doi: 10.3390/rs11111277.

[23] Z. Yifu, "Design of track tracking controller for tracked car based on pure tracking algorithm," in *Proc. IEEE 2nd Int. Conf. Elect. Eng., Big Data Algorithms*, 2023, pp. 1765–1770.

[24] F. Wang, F. Xu, and Y.-Q. Jin, "Three-dimensional reconstruction from a multiview sequence of sparse ISAR imaging of a space target," *IEEE Trans. Geosci. Remote Sens.*, vol. 56, no. 2, pp. 611–620, Feb. 2018.

[25] Y. Zhou, L. Zhang, Y. Cao, and Y. Huang, "Optical-and-radar image fusion for dynamic estimation of spin satellites," *IEEE Trans. Image Process.*, vol. 29, pp. 2963–2976, Nov. 2019.

[26] L. Liu, F. Zhou, X.-R. Bai, M.-L. Tao, and Z.-J. Zhang, "Joint cross-range scaling and 3D geometry reconstruction of ISAR targets based on factorization method," *IEEE Trans. Image Process.*, vol. 25, no. 4, pp. 1740–1750, Apr. 2016.

[27] G. Li, J. Zou, S. Xu, B. Tian, and Z. Chen, "A method of 3D reconstruction via ISAR sequences based on scattering centers association for space rigid object," *Proc. SPIE*, vol. 9252, 2014, Art. no. 92520N.

[28] G. Li, Y. Liu, L. Wu, S. Xu, and Z. Chen, "Three-dimensional reconstruction using ISAR sequences," *Proc. SPIE*, vol. 8919, 2013, Art. no. 891908.

[29] F. E. McFadden, "Three-dimensional reconstruction from ISAR sequences," *Proc. SPIE*, vol. 4744, pp. 58–67, 2002.

[30] L. Liu, Z. Zhou, F. Zhou, and X. Shi, "A new 3-D geometry reconstruction method of space target utilizing the scatterer energy accumulation of ISAR image sequence," *IEEE Trans. Geosci. Remote Sens.*, vol. 58, no. 12, pp. 8345–8357, Dec. 2020.

[31] H. Kang, J. Li, Q. Guo, and M. Martorella, "Pattern coupled sparse Bayesian learning based on UTAMP for robust high resolution ISAR imaging," *IEEE Sensors J.*, vol. 20, no. 22, pp. 13734–13742, Nov. 2020.

[32] H. Kang, J. Li, Q. Guo, M. Martorella, E. Giusti, and J. Cai, "Robust interferometric ISAR imaging with UAMP-based joint sparse signal recovery," *IEEE Trans. Aerosp. Electron. Syst.*, vol. 59, no. 4, pp. 3890–3906, Aug. 2023, doi: 10.1109/TAES.2022.3233545.

[33] J. Wang, Y. Li, and M. Song, "Satellite attitude estimation based on ISAR image sequence interpretation," in *Proc. CIE Int. Conf. Radar*, 2021, pp. 2484–2487, doi: 10.1109/Radar53847.2021.10027878.

[34] L. Yang et al., "Integration of rotation estimation and high-order compensation for ultrahigh-resolution microwave photonic ISAR imagery," *IEEE Trans. Geosci. Remote Sens.*, vol. 59, no. 3, pp. 2095–2115, Mar. 2021.

[35] Y. Gao, M. Xing, Y. Li, W. Sun, and Z. Zhang, "Joint translational motion compensation method for ISAR imagery under low SNR condition using dynamic image sharpness metric optimization," *IEEE Trans. Geosci. Remote Sens.*, vol. 60, Dec. 2021, Art. no. 5108515.

Dan Xu received the B.S. and Ph.D. degrees in electrical engineering from Xidian University, Xi'an, China, in 2014 and 2020, respectively.

From 2019 to 2020, she did research work as a joint training Ph.D. student with the Department of Electrical Engineering, Parthenope University, Napoli, Italy. She is currently a Lecturer with the Academy of Advanced Interdisciplinary Research, Xidian University.

Xuan Wang was born in Shaanxi Province, China, in 1997. He received the B.S. degree in electronic and information engineering from Xidian University, Xi'an, China, in 2019 where he is currently working toward the Ph.D. degree in optical engineering with the School of Optoelectronic Engineering.

His current research interests include radar signal processing, synthetic aperture radar, and inverse synthetic aperture radar imaging.

Zhixin Wu (Graduate Student Member, IEEE) was born in Shangrao, China, in 1999. He received the B.S. degree in electronic and information engineering from Xidian University, Xi'an, China, in 2020, where he is currently working toward the Ph.D. degree in signal and information processing with the National Laboratory of Radar Signal Processing.

His research interests include electromagnetic scattering calculation, signal processing, and ISAR imaging.

Jixiang Fu (Member, IEEE) received the B.S. and Ph.D. degrees in signal and information processing subject from Xidian University, Xi'an, China, in 2014 and 2021, respectively.

He is with the Academy of Advanced Interdisciplinary Research, Xidian University, Xi'an, China. From 2019 to 2021, he was a Visiting Student with Villanova University, Villanova, PA, USA. He is currently a Lecturer with the Academy of Advanced Interdisciplinary Research, Xidian University, Xi'an, China. His research interests include inverse synthetic aperture radar motion compensation and imaging algorithm development, and wide-angle radar imaging and 3-D imaging.

Yuhong Zhang was born in Shaanxi, China, in 1987. She received the B.S. degree in communications engineering from the Harbin University of Science and Technology, Harbin, China, in 2009, and the M.Sc. and Ph.D. degrees in signal and information processing subject from Xidian University, Xi'an, China, in 2012 and 2018, respectively.

Her major research interests include radar imaging (synthetic aperture radar/inverse synthetic aperture radar) and compressive sensing.

Jianlai Chen (Senior Member, IEEE) was born in Hengyang, Hunan, China, in 1990. He received the B.S. degree in electronic engineering and the Ph.D. degree in signal and information processing from Xidian University, Xi'an, China, in 2013 and 2018, respectively.

He is currently an Associate Professor with Central South University, Changsha, China. He has authored or coauthored two books and more than 30 research articles in high-impact peer-reviewed journals. His research interests include synthetic aperture radar (SAR) imaging, SAR motion compensation and autofocus, electronic reconnaissance, and machine learning.

Dr. Chen serves as an Associate Editor for the *IEEE Journal on Miniaturization for Air and Space Systems*. He also serves as the Guest Editor for the Special Issues of the *IEEE Journal of Selected Topics in Applied Earth Observations and Remote Sensing* and *MDPI Remote Sensing*. He has reviewed more than 100 manuscripts for IEEE journals.

Mengdao Xing (Fellow, IEEE) received the B.S. and Ph.D. degrees in signal and information processing subject from Xidian University, Xi'an, China, in 1997 and 2002, respectively.

He is currently a Professor with the National Laboratory of Radar Signal Processing, Xidian University. He holds the appointment of Dean of the Academy of Advanced Interdisciplinary Research Department, Xidian University. His current research interests include synthetic aperture radar (SAR), SAR interferometry, inversed SAR, sparse signal processing, and microwave remote sensing. He has written or cowritten more than 200 refereed scientific journal papers. He also has authored or coauthored two books about SAR signal processing. The total citation times of his research are greater than 10 000 (H-index 50). He was rated as the most cited Chinese researcher by Elsevier. He has achieved more than 50 authorized China patents. His research has been supported by various funding programs, such as the National Science Fund for Distinguished Young Scholars. He has held several Special Issues on the IEEE GRSM and JSTARS. He currently serves as the Associate Editor for radar remote sensing of IEEE TRANSACTIONS ON GEOSCIENCE AND REMOTE SENSING and the Editor-in-Chief for *MDPI Sensors*.